INTERNATIONAL JOURNAL FOR NUMERICAL METHODS IN FLUIDS
Int. J. Numer. Meth. Fluids 2000; **33**: 405–427

A finite element method for free surface flows of incompressible fluids in three dimensions. Part II. Dynamic wetting lines

Thomas A. Baer[a], Richard A. Cairncross[b,*], P. Randall Schunk[a], Rekha R. Rao[a] and Phillip A. Sackinger[a]

[a] *Sandia National Laboratories, Albuquerque NM, U.S.A.*
[b] *Chemical Engineering Department, Drexel University, Philadelphia, PA, U.S.A.*

SUMMARY

To date, few researchers have solved three-dimensional free surface problems with dynamic wetting lines. This paper extends the free surface finite element method (FEM) described in a companion paper [Cairncross RA, Schunk PR, Baer TA, Sackinger PA, Rao RR. A finite element method for free surface flows of incompressible fluid in three dimensions. Part I. Boundary fitted mesh motion. *International Journal for Numerical Methods in Fluids* 2000; **33**: 375–403] to handle dynamic wetting. A generalization of the technique used in two-dimensional modeling to circumvent double-valued velocities at the wetting line, the so-called kinematic paradox, is presented for a wetting line in three dimensions. This approach requires the fluid velocity normal to the contact line to be zero, the fluid velocity tangent to the contact line to be equal to the tangential component of web velocity, and the fluid velocity into the web to be zero. In addition, slip is allowed in a narrow strip along the substrate surface near the dynamic contact line. For realistic wetting line motion, a contact angle that varies with wetting speed is required because contact lines in three dimensions typically advance or recede at different rates depending upon location and/or have both advancing and receding portions. The theory is applied to capillary rise of static fluid in a corner, the initial motion of a Newtonian droplet down an inclined plane, and extrusion of a Newtonian fluid from a nozzle onto a moving substrate. The extrusion results are compared with experimental visualization. Copyright © 2000 John Wiley & Sons, Ltd.

KEY WORDS: contact lines; finite element method; free surface; pseudo-solid mesh motion; simulation; three-dimensional; wetting lines

1. INTRODUCTION

Even with a powerful numerical method of predicting free and moving boundary problems in three dimensions [1], modeling practical problems with dynamic contact lines poses many outstanding challenges. These contact lines represent the curve in three-dimensional space

* Correspondence to: Chemical Engineering Department, Drexel University, 32nd & Chestnut Streets, Philadelphia, PA 19104, U.S.A.

Received 26 October 1998
Revised 29 June 1999

where liquid, gas, and solid meet. Wetting problems involve dynamic contact lines in which the liquid is displacing the gas, or vice versa, along the solid surface. The approaches for treating dynamic contact lines in two dimensions are not easily extended to three dimensions, both conceptually and practically.

Wetting phenomena are often categorized as *static* or *dynamic*. Dynamic wetting involves the relative motion of a fluid/solid/gas contact line and a solid that is *forced* by a large relative velocity (i.e., plunging a substrate rapidly into a quiescent pool of liquid) or *spontaneous* by the propensity of the liquid/gas/solid system to lower its free energy by advancing or receding on a surface. Contact lines within all of these classes are common in manufacturing processes, like continuous liquid film coating (forced wetting), soldering and brazing (forced and spontaneous), flow in porous media (forced and spontaneous displacement), and many other technologically important areas. For decades researchers have attempted to contrive continuum models that are useful to engineering analysis, which simulate the true physics; however, all of the models have implementation aspects that have been simplified to two dimensions, where a true contact line becomes a point. At that point, the theoretical treatment of wetting is categorically static or dynamic, a classification that greatly simplifies implementation in a model. In three dimensions it is often the case to have both of these extremes active along a single contact line, and even worse, the local wetting regime will span a large range of local capillary numbers, from static to dynamic. In this paper we present generalizations of what is well established as acceptable *ad hoc* procedures for modeling static and dynamic contact lines in two dimensions so that they can be applied in three-dimensional situations.

The physical differences between static and dynamic wetting regimes are important to the approach taken here. Static wetting lines at which two fluids (usually gas and liquid) meet at a fixed curve on a solid boundary are nicely described from a hydrodynamic viewpoint as a nearly stagnant region at which the fluid mechanics are unimportant, i.e., typically trivial Dirichlet conditions on the velocity components suffice. A static contact angle can be considered a thermodynamic property [2], although it may be a complex function of the underlying chemical make-up and structure of the surface, which often leads to hysterisis effects. Dynamic wetting lines at which one fluid displaces the other along the solid boundary are another matter. A dynamic wetting angle is not a thermodynamic property, but the result of a complex interplay of a variety of non-equilibrium processes. First and foremost are the local hydrodynamics around an advancing or receding wetting line. Those hydrodynamics include both the fluid mechanics in the displacing fluid and in the receding fluid. Then there are the surface tension-related phenomena on the fluid–fluid interface near the contact line. The usual static wetting forces are present at low capillary numbers, and there is the possibility of surface gradients due to the presence of surface active species or temperature gradients. Finally, somewhere and somehow near the three-phase line some mechanism equivalent to fluid slip on the solid surface must be operative in order to relieve the otherwise singular stress that would result (the so-called rolling motion regime is an exception [3]).

The mathematical condition that is used most often in computational analysis of free surface flows for determining the surface position is the so-called kinematic surface condition [1]. Local surface kinematics near a dynamic contact line as governed by this condition have important implications on speed of the liquid parcels on the surface and those adhered to the substrate around a dynamic contact line. Without evaporation, the kinematic condition

demands that the air–liquid surface be a material stream surface right up to the contact line. If the liquid cannot penetrate the solid, as is usually the case, an additional condition of impenetrability must be applied. For both of these conditions to be true, the liquid velocity immediately at the wetting line and the velocity of the wetting line itself must be the same. For steady flow in two dimensions this implies zero velocity. However, the velocity at the contact line must also be the substrate velocity if no-slip is enforced to include the contact line. This situation of double-valued velocities has been termed the 'kinematic paradox', as coined by Kistler [4], and is a situation that demands some liquid slip at the moving solid surface. Only for the case of a 180° contact angle is it possible to satisfy all conditions at the contact line simultaneously. This situation is often referred to as the rolling motion condition [3]. For angles other than 180°, researchers have adopted several approaches in finite element or finite difference applications as discussed below.

The most common approach restricts the analysis to conventional continuum theory at macroscopic length scales. It removes the multi-valued velocity at the wetting line by *ad hoc* boundary conditions that allow slip at the line (i.e., the liquid velocity at the wetting line is the same as that of the line) and partial slip nearby, and prescribes a contact angle that is supposed to represent an apparent dynamic contact angle of the sort observed in experiments, possibly taken from an empirical correlation. This approach permits computed prediction of realistic wetting processes [5]. There are many pitfalls to this approach, which should be considered (see Christodoulou *et al*. [6]), but nonetheless it is this approach we extend here to three dimensions. It is true, for instance, that the mesh refinement required to resolve this set of conditions is exceedingly large, especially in three dimensions, and this casts some doubt to the accuracy of the angle being applied, as the microscopic angle may be drastically different.

Other approaches have overcome the need to specify perfect slip at the putative wetting line by exploiting the weak form of the Galerkin weighted residual equations [4] or by taking advantage of collapsed elements that give multiple coincident nodes at the contact line [7; Christodoulou KN, Scriven LE. Singular elements at dynamic wetting lines. Unpublished 1990]. Although these techniques work well in two dimensions, they undermine severely the mesh convergence of the flow field around the contact line and are impractical in three dimensions due to difficulties in mesh generation and manipulation along a three-dimensional contact line (perhaps the double-valued velocity at the contact line achieved with collapsing elements is a possibility).

Two other approaches are worthy of mention. The first adheres to the use of standard *ad hoc* boundary conditions at a contact line, i.e., prescribed contact angle and local slip flow, but imposes a sub-microscopic static angle and systematically refines the mesh to permit a local analysis [8–10]. This procedure works well for a small capillary number, but is limited at larger ones. This limitation is unfortunate as the approach shows promise in three dimensions. The second approach seeks to resolve the sub-microscopic physics of dynamic wetting. It incorporates a refined model for the local air displacement mechanism right into a macroscopic computation, and thereby attempts to provide realistic boundary conditions for the macroscopic flows. Some have attempted this approach at realistic conditions [11] but the challenges of dealing with meshing distortion in three dimensions are enormous.

To date there have been several significant published works in three dimensions that are important to mention here, as they set an important precedent. Dimitrakopoulos and Higdon

[On the displacement of three-dimensional fluid droplets from solid surfaces in low-Reynolds number shear flows. *Journal of Fluid Mechanics* 1998; **377**: 189–222] employed boundary element formulations to determine the configuration of a three-dimensional droplet just prior to motion. An experimental work by Extrand and Kumagai [12] considered a similar topic. Two related papers [13,14] sought perturbation solutions to finding the shape of a droplet down an inclined plane with and without hysteresis in the contact angle model. Finally, a recent theoretical paper by Schwartz and Eley [15] presents a technique for simulating the motion of very small droplets on heterogeneous surfaces where surface tension forces dominate.

In the first section below we begin with a generalization of the so-called kinematic paradox to three-dimensional contact line motion. Although obvious in hindsight, the implementation requires a variable contact angle model. We formulate a linear relation between the local contact angle and the local wetting speed, or local capillary number. This model or the equivalent is necessary in nearly every situation as the local wetting speed often varies greatly along a moving contact line, even diminishing to a point at which the line becomes static relative to the moving surface. The next section discusses implementing these concepts and models into a Galerkin finite element code. Finally, we present three examples to demonstrate the new model The first involves the capillary rise of fluid in a corner geometry, the second the motion of a drop down an inclined surface, and the third the lay-down of a liquid bead on a moving substrate. The important feature of the last two problems is that the wetting regimes vary from static to dynamic along the contact line.

2. PHYSICAL THEORY OF A WETTING LINES IN THREE DIMENSIONS

2.1. The kinematic paradox in two dimensions

In two dimensions the contact line is represented as a single point where the free surface intersects a moving substrate boundary. The kinematic condition imposed on the free surface imposes a purely tangential flow velocity along it. The impenetrability and no-slip constraints associated with the moving substrate impose a fluid velocity at the contact line that is parallel to the substrate boundary. For any contact angle other than 180°, these two requirements are incompatible and require that two velocities exist at the contact line in order to satisfy both simultaneously. This incompatibility is often referred to as the 'kinematic paradox'. It is a paradox in the sense that a fluid particle arriving at the wetting line will be faced with two possible velocities and hence two possible future trajectories. Because conventional models of fluid flow do not typically consider this possibility, the result is a singularity in fluid stress when an attempt is made to apply them at the wetting line.

To resolve this paradox, it is often suggested that there are wetting forces locally near the contact line (on the sub-grid scale), which induce a spreading velocity of the fluid, which, at steady state, exactly cancels the motion of the substrate and results in zero velocity of the fluid in the fixed frame of reference when viewed on the scale of the problem. In effect, this model of wetting phenomena does not attempt to resolve the intricate details of the wetting zone regions, but instead recognizes that from a sufficient distance the motion of the fluid at the

contact line has little influence elsewhere and therefore can be considered stationary. However, since the fluid at the wetting line now has a velocity different from the substrate, it is necessary to also include a region near the wetting line where slip is permitted. The next section extends this notion to a three-dimensional wetting line.

2.2. Generalization to a contact line in three dimensions

Figure 1 shows a typical free surface geometry near the wetting line. The web surface has a normal vector, $\boldsymbol{n}_w$, and is moving at velocity $\boldsymbol{u}_w$. The free surface intercepts the substrate at a dynamic contact line with unit normal and tangent vectors, $\boldsymbol{n}_{cl}$ and $\boldsymbol{t}_{cl}$, both of which are orthogonal to $\boldsymbol{n}_w$, i.e., in the plane of the substrate.

To circumvent the kinematic paradox in three dimensions, we recognize that, as in two dimensions, slipping of the fluid at the contact line must be permitted; we define the wetting velocity, u_{wet} to be the normal component of the fluid velocity at the contact line relative to the substrate

$$u_{wet} = \boldsymbol{n}_{cl} \cdot (\boldsymbol{u} - \boldsymbol{u}_w) \tag{1}$$

We assume that the wetting velocity in three dimensions is the same as the wetting velocity under similar conditions in two dimensions and that curvature effects are negligible along the contact line. Because the contact line is curved in three dimensions, the wetting speed must vary along the contact line, as discussed below.

For steady state problems, the wetting velocity is equal in magnitude but opposite in sign to the component of the substrate velocity normal to the wetting line, or

$$u_{wet} = -\boldsymbol{n}_{cl} \cdot \boldsymbol{u}_w \tag{2}$$

that is, the fluid wets outward as fast as the substrate carries it in. It is this condition that permits a smooth transition along the wetting line from dynamic behavior to static behavior, where the substrate moves parallel to the wetting line and the wetting velocity is zero. When Equation (2) is substituted into Equation (1), it is found that the fluid velocity at the contact line, $\boldsymbol{u}$, does not have a component normal to the contact line

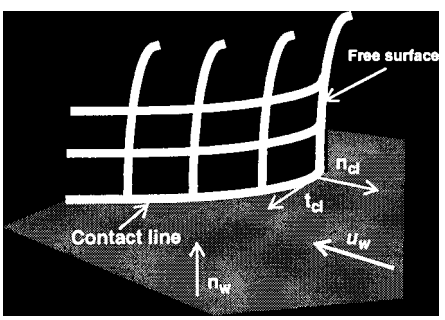

Figure 1. Schematic of general three-dimensional dynamic wetting line with vector definitions.

$$\boldsymbol{n}_{\mathrm{cl}} \cdot \boldsymbol{u} = 0 \tag{3}$$

We call this the *edge kinematic* condition for steady state problems. Recall that $\boldsymbol{n}_{\mathrm{cl}}$ is a unit vector normal to the wetting line in the plane of the substrate.

An additional assumption is that the fluid slips only normal to the contact line and does not slip tangentially. More precisely, the physics of wetting at the wetting line do not induce tangential velocity in the fluid, which is different from the tangential velocity of the substrate. Thus

$$\boldsymbol{t}_{\mathrm{cl}} \cdot \boldsymbol{u} = \boldsymbol{t}_{\mathrm{cl}} \cdot \boldsymbol{u}_{\mathrm{w}} \tag{4}$$

By this equation, the fluid velocity tangent to the contact line varies with the contact line orientation and once again permits smooth transition from a dynamic wetting line to a static wetting line, where the fluid at the wetting line moves with the same velocity as the substrate.

Finally, in most problems of interest, the fluid does not penetrate into the substrate

$$\boldsymbol{n}_{\mathrm{w}} \cdot \boldsymbol{u} = 0 \tag{5}$$

Equations (3)–(5) constitute three constraints on the velocity that replace the fluid momentum equation along the contact line in steady state problems and allow us to resolve the paradox. However, they apply only when the contact line is not moving in time. In transient problems, the model of the wetting velocity must now include the normal component of the mesh velocity at the contact line, $\dot{\boldsymbol{x}}_{\mathrm{fs}}$

$$u_{\mathrm{wet}} = -\boldsymbol{n}_{\mathrm{cl}} \cdot \boldsymbol{u}_{\mathrm{w}} + \boldsymbol{n}_{\mathrm{cl}} \cdot \dot{\boldsymbol{x}}_{\mathrm{fs}} \tag{6}$$

and Equations (3)–(5) generalize as follows:

$$\boldsymbol{n}_{\mathrm{cl}} \cdot (\boldsymbol{u} - \dot{\boldsymbol{x}}_{\mathrm{fs}}) = 0, \quad \boldsymbol{t}_{\mathrm{cl}} \cdot \boldsymbol{u} = \boldsymbol{t}_{\mathrm{cl}} \cdot \boldsymbol{u}_{\mathrm{w}}, \quad \text{and} \quad \boldsymbol{n}_{\mathrm{w}} \cdot (\boldsymbol{u} - \dot{\boldsymbol{x}}_{\mathrm{fs}}) = 0 \tag{7}$$

The tangential motion of the mesh at the contact line has no physical meaning and so is left out of the tangential constraint on the fluid velocity. It is clear that the transient relations reduce to the steady state relations when $\dot{\boldsymbol{x}}_{\mathrm{fs}} = 0$.

2.3. Variable contact angles for three-dimensional dynamic contact lines

To illustrate and test the requirements for a three-dimensional contact line model, we consider a droplet of fluid descending an inclined plane at a constant velocity. At the leading edge of the droplet, the contact line is *advancing* with respect to the substrate at a constant velocity. At the trailing edge, the contact line is *receding* at the same constant velocity. At all other points, the contact line advances or recedes normal to itself at velocities that are some fraction of the overall speed of descent. There are at least two points where it neither advances nor recedes (in the normal direction). Assuming a constant wetting speed around the edge of the droplet would result in an unrealistic prediction of a droplet the spreads without bound.

Furthermore, there is a wealth of experimental evidence that, for a given fluid in contact with a given substrate, indicates the dynamic contact angle is most dependent upon its rate of advance or recession (see Blake and Ruschak [16]). This rate can be expressed as the normal component of the relative velocity of the free surface at the contact line and the substrate

$$\dot{x}_{\text{wet}} = \boldsymbol{n}_{\text{cl}} \cdot (\dot{\boldsymbol{x}}_{\text{fs}} - \boldsymbol{u}_{\text{w}}) \tag{8}$$

Therefore, all things being equal, the contact angle at any point on the contact line is a function of $\dot{\boldsymbol{x}}_{\text{wet}}$ and the hydrodynamic properties of the fluid

$$\theta = f(\dot{x}_{\text{wet}},\ Ca) \tag{9}$$

θ is the dynamic contact angle as illustrated in Figure 2 and $Ca = \mu V/\sigma$ is the capillary number based on a reference velocity V. Thus, the contact angle varies along the contact line. This fact can be easily observed by studying the motion of a raindrop down a windshield and has been suggested previously by other researchers [13; Dimitrakopoulos P, Higdon JJL. Submitted]. It is perhaps noteworthy that Equation (8) is nearly identical to Equation (6) suggesting an alternative statement of the wetting line model would be $u_{\text{wet}} = \dot{x}_{\text{wet}}$.

We define a local capillary number, Ca_{L}, which varies along the wetting line, as

$$Ca_{\text{L}} = Ca\,\frac{\dot{x}_{\text{wet}}}{V} = Ca\,\boldsymbol{n}_{\text{cl}} \cdot \left(\frac{\dot{\boldsymbol{x}}_{\text{fs}} - \boldsymbol{u}_{\text{w}}}{V}\right) \tag{10}$$

With this definition, an advancing wetting line corresponds to $Ca_{\text{L}} > 0$, while a receding line corresponds to $Ca_{\text{L}} > 0$. Reports in the literature propose many different relationships between dynamic contact angle and wetting speed; they are normally expressed in terms of the capillary number. The results are typically for two-dimensional flow systems so there is usually only a single capillary number associated with the entire contact line. In addition, the results often only apply to advancing or receding contact lines, or apply only over a limited range of capillary numbers, e.g., References [17–19]. To ensure computational robustness a relation is needed that is applicable simultaneously to advancing and receding contact lines and is valid over a large range of capillary numbers. Such a correlation was not immediately available in the literature. Indeed there is evidence that measured dynamic contact angles are also

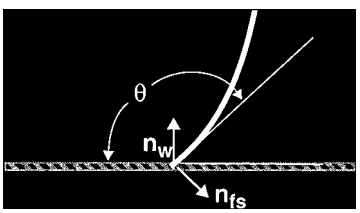

Figure 2. Schematic depiction of local contact angle with substrate and free surface normals.

dependent upon the flow geometry itself [20]. Thus, a correlation developed for contact angles from a plunging tape device, for example, might not be appropriate for other problems.

Instead, we used an admittedly simplistic but computationally tractable linear model, as suggested by Kister [21]

$$n_{\mathrm{w}} \cdot n_{\mathrm{fs}} = \cos\theta = \cos\theta_{\mathrm{s}} - c_T Ca_{\mathrm{L}} = \cos\theta_{\mathrm{s}} - c_T Ca \frac{\dot{x}_{\mathrm{wet}}}{V} \tag{11}$$

θ is the contact angle, θ_{s} is the static contact angle (when $\dot{x}_{\mathrm{wet}} = 0$), and c_T is a proportionality constant. The vectors n_{w} and n_{fs} and the contact angle are depicted in Figure 2 for a two-dimensional contact line. Note that Equation (11) can also be used to set a fixed contact angle by setting $c_T = 0$.

Equation (11) is strictly applicable only for $|Ca_{\mathrm{L}}| \ll 1$. It is also hampered because it can predict contact angles that are greater than 180° or less than 0°. Furthermore, this model does not account for certain well-known phenomena, like contact angle hysteresis or critical contact angles. However, the primary goal of this current work was the development of an effective and efficient method for finding the solution of problems with three-dimensional dynamic contact lines. The linear model provides the essential features of varying contact angles and wetting speeds while being easy to implement computationally. In the future the linear model could be generalized.

3. FINITE ELEMENT FORMULATION

Part I [1] of this two-paper series provides details of the governing partial differential equations and corresponding finite element formulation. The description is extended here to include the application of boundary conditions specific to dynamic wetting lines.

Over the portion of the solid substrate in contact with the liquid, except for a thin region near the dynamic contact line, we assume no-slip between the substrate and the fluid. The no-slip conditions are applied as Dirichlet conditions. In a thin region of the solid substrate boundary near the dynamic contact line we allow tangential slip using the Navier slip condition

$$\boldsymbol{n}_{\mathrm{w}} \cdot \boldsymbol{T} \cdot \boldsymbol{t} = \frac{1}{\gamma} (\boldsymbol{u} - \boldsymbol{u}_{\mathrm{w}}) \cdot \boldsymbol{t} \tag{12}$$

The weighted residual of Equation (12)

$$\int_A \phi_i \boldsymbol{e}_\beta \boldsymbol{n} \colon \boldsymbol{T}_{\mathrm{in}} \, \mathrm{d}A = \int_A \phi_i \frac{1}{\gamma} \boldsymbol{e}_\beta \cdot (\boldsymbol{u} - \boldsymbol{u}_{\mathrm{w}}) \, \mathrm{d}A \tag{13}$$

replaces the boundary term appearing in the weak form of the momentum equation described in Part I [1]. Note that the normal component of Equation (13) is never used because the impenetrability constraint (5) replaces the normal component of the momentum equation that contains it.

A planar shape of the solid substrate boundary is imposed by a plane condition as discussed in Part I [1]

$$R_i^{\mathrm{d},n} = ax_i + by_i + cz_i + d \tag{14}$$

Along the dynamic contact line, three boundary conditions are needed on both the fluid momentum equation and the pseudo-solid mesh motion equation. Equations (7) replace the three components of the momentum equation on the dynamic contact line. These equations represent no-penetration into the substrate, no-slip tangential to the contact line, and the edge kinematic condition. Because all three components of the momentum equation are replaced by boundary conditions, rotation of the momentum equation at the contact line is not necessary. The impenetrability condition is applied as a Dirichlet condition; i.e., the velocity component normal to the substrate is explicitly set to zero. The no-tangential slip condition and edge kinematic condition are applied as point collocated boundary conditions at Gauss integration points along the contact line, i.e., the boundary conditions are evaluated at these discrete points along the contact line of the element edge and used to replace the fluid momentum equations of the nodes on the element edge.

The contact angle condition of Equation (11) and the geometric shape of the substrate (as in Equation (14)) constrain the mesh motion along the contact line. To allow the mesh to redistribute tangentially along the contact line, we rotate the components of the pseudo-solid mesh motion equations into components normal to the substrate, tangent to the contact line, and binormal to the contact line (outward pointing normal in plane of substrate)

$$\begin{bmatrix} R_i^{\mathrm{n}} \\ R_i^{\mathrm{t}} \\ R_i^{\mathrm{b}} \end{bmatrix} = \begin{bmatrix} \boldsymbol{n}_{\mathrm{w},i}^T \\ \boldsymbol{t}_{\mathrm{cl},i}^T \\ \boldsymbol{n}_{\mathrm{cl},i}^T \end{bmatrix} \begin{bmatrix} R_i^x \\ R_i^y \\ R_i^z \end{bmatrix} \tag{15}$$

$\boldsymbol{n}_{\mathrm{w},i}$ is a vector normal to the substrate surface at node i, $\boldsymbol{t}_{\mathrm{cl},i}$ is vector tangent to the dynamic contact line, and $\boldsymbol{n}_{\mathrm{cl},i} = \boldsymbol{n}_{\mathrm{w},i} \times \boldsymbol{t}_{\mathrm{cl},i}$ is a binormal vector that is perpendicular to both $\boldsymbol{n}_{\mathrm{w}}$ and $\boldsymbol{t}_{\mathrm{cl}}$ and outward pointing from the wetting line in the substrate surface. Part I [1] discusses the calculation of these nodal unit vectors.

Along the dynamic contact line, the normal component of the rotated pseudo-solid mesh motion equation is replaced by the planar boundary condition (14) as discussed in Part I [1]. The contact angle condition (11) is applied as a weighted residual equation integrated along the contact line

$$\int_S \phi_i(\cos\theta - (\cos\theta_{\mathrm{s}} - c_T Ca_{\mathrm{L}}))\,\mathrm{d}S = 0 \tag{16}$$

This weighted residual replaces the binormal component of the pseudo-solid mesh motion equation. The local capillary number is calculated according to Equation (10). We retain the remaining tangential component of the rotated pseudo-solid momentum equation to allow the nodes to slide freely along the dynamic contact line. If this step is omitted, spurious sources of mesh stress will be introduced at the contact line.

4. RESULTS

4.1. Capillary rise in a corner

When a fluid wets the walls of its container, the meniscus rises near the wall to balance gravitational and capillary forces. Results of the meniscus shape are well tabulated for two-dimensional problems, where the free surface is a curve. Brown [22] and others have calculated the shapes of menisci for three-dimensional problems without gravity, where the mean curvature is constant. We use capillary rise with gravity as a simple test problem for the contact angle formulation discussed above. Figure 3 shows predictions of the meniscus shape for capillary rise in a box at various contact angles. The container is a box with smooth, vertical walls; the solution is obtained for quarter of the box by imposing symmetry at the vertical mid-planes. There is no-slip of the fluid on the box walls, and at steady state the velocity is zero everywhere within numerical accuracy. The bottom of the box is an open boundary with a specified pressure; this pressure and the external pressure determine the depth of liquid in the box ($\Delta p = \rho g h$).

The top surface of the fluid is the free surface that moves to balance capillary and pressure forces via the capillary condition and to conserve mass via the kinematic condition. The side walls, symmetry planes, and bottom boundary restrict the mesh position by geometric plane conditions. The free surface intersects the symmetry planes at a right angle and intersects the walls at specified contact angles. In the corner where the walls meet, two contact angle conditions, two geometric planar conditions, and the kinematic condition all apply to the mesh equation at the same point. However, only three independent boundary conditions can apply to the pseudo-solid mesh motion equation at any point, so two of the boundary conditions need to be eliminated there. We tested several choices of boundary conditions at this corner and determined that the most effective method is to apply both the geometric planar constraints and the kinematic condition. Nevertheless, the contact angle conditions are still well satisfied up to the corner.

The predictions in Figure 3 show that the meniscus rises near the walls due to fluid wetting but becomes nearly flat at the center of the box. The meniscus rises highest in the corner due to additional curvature from bending the rising meniscus around the corner, i.e., near the

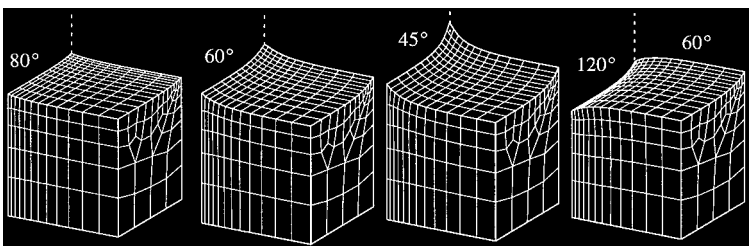

Figure 3. Predictions of capillary rise in a box with various values of the contact angle between the free surface and the walls of the box. The pressure distribution is hydrostatic. Contact angles are labeled on each plot.

corner the second radius of curvature contributes significantly to the pressure drop across the interface. Far from the corner, the second radius of curvature is nearly infinite and the meniscus shape approaches that of a translationally symmetric interface. As the contact angle decreases (fluid wets solid better), the fluid wicks higher onto the walls and into the corner.

The contact angles on the two walls do not have to be equal. Figure 3 shows the capillary rise near a corner between two walls with contact angles of 60° and 120°. In this case, fluid rises on the wall with a contact angles of 60° and descends on the wall with contact angle of 120°. In the corner where the walls meet, the meniscus height is equal to the height of the meniscus at the center of the box. This is a simple example demonstrating the application of our contact angle formulation to three-dimensional free surface problems. In the next two sections we apply the formulation to problems with fluid flow.

4.2. Initial motion of droplet down an inclined plane

The motion of a droplet down an inclined plane is a problem that, despite its prosaicness, has not received much attention. Dussan and Chow [13] developed perturbation solutions valid for small capillary numbers, contact angles, and inclinations to the critical configuration for motion and the configuration for steady state motion. Later, Dussan [14] extended this work for arbitrary contact angles. Dimitrakopoulos and Higdon (submitted) used boundary element methods to also compute the critical configuration prior to motion.

The contact line conditions discussed previously have been applied to the motion of an initially quiescent droplet down an inclined plane. Figure 4 shows the initial droplet shape and the finite element mesh employed in the solution. This configuration was obtained from an

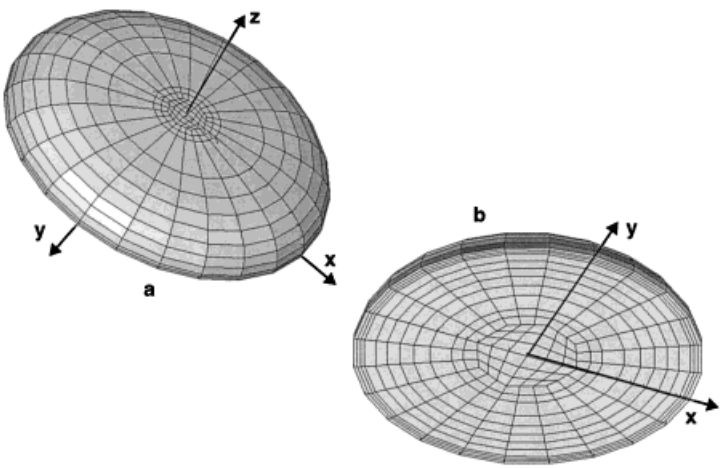

Figure 4. Mesh and starting configuration of droplet motion calculation. Note that (a) is an oblique view from above of the drop's upper surface; (b) is an oblique view from below of the drop's underside. We note that actual computational domain differs from this figure in that only the domain for which $y \geq 0$ was used as discussed in the text.

originally hemispherical shape. A gravitational acceleration was applied along the z-axis and the droplet was allowed to deform over time to the final shape shown in Figure 4. The computational domain used was actually only half of the region shown in Figure 4, since the $x = 0$ plane was taken as a symmetry plane. This had the benefit of reducing the number of unknowns for this lengthy transient calculation and also provided determinacy to the mesh displacement unknowns. Without this step, unphysical rotary modes of mesh motion about the z-axis could appear in the phase of the calculation when there was no inclination.

The free surface of the droplet is subject to the kinematic constraint

$$\boldsymbol{n} \cdot (\boldsymbol{u} - \dot{\boldsymbol{x}}_{\mathrm{fs}}) = 0 \tag{17}$$

No-slip was enforced on the underside of the droplet, except in a narrow annular band of elements adjacent to the contact line. On these elements, the Navier slip condition (12) was employed. Its purpose was to permit transition from the no-slip condition in the interior to the contact line velocity conditions described in an earlier section. The slip coefficient, γ, was taken as 0.01.

During the computation it became necessary to 'anneal' the mesh. It was observed that as the droplet moved further and further from its starting point, the larger and larger displacements would begin to inhibit convergence of the iterative solver. It was, therefore, necessary periodically to update the co-ordinates of each node with its respective displacement vector and restart the problem with a zero displacement field, effectively removing the mesh stresses. The velocity and pressure fields, however, were not changed. This is a viable procedure because ultimately it is the position of the mesh nodes and not their displacement from a reference state that interacts with the other unknown fields.

On the contact line, the momentum equations were replaced by the three conditions given in (7). Since the substrate is motionless for this transient problem, the web speed, u_{w}, was set to zero. This linear relationship between the contact angle and the local capillary number (11) was used to determine the local contact angle. For this example calculation, *ad hoc* values for the parameters in this model were chosen. The static contact angle θ_{s} was set at 90° and the linear constant c_T at 0.99. The latter value is somewhat meaningless but for the fluid modeled it would result in a 180° contact angle at a droplet speed of 720 cm s^{-1}. Thus, the contact line is fairly slippery.

The fluid modeled had physical properties similar to water: $\rho = 1$ g cm^{-3}, $\mu = 0.1$ dyn s cm^{-2}, and $\sigma = 72$ dyn cm^{-1}. The viscosity is roughly ten times that of water at room temperature and this value was chosen to mitigate inertial effects on the mesh distortion in the initial computation from the hemisphere to the stable deformed shape.

At time zero, a gravitational acceleration vector is rotated 30° towards the x-axis, i.e., the substrate is tipped 30° downward in the x-direction. The subsequent motion is depicted in Figure 5, which shows side and planform views of the droplet at several times. Note the size of the grid scale. Overall fluid tends to shift to its downhill side and the droplet becomes elongated longitudinally. Ultimately, a 'rooster tail' appears in the free surface at the trailing edge. This more than likely is the distortion in the mesh in this region. A remeshing of the domain would be required to continue. This was not done.

4.3. Laydown of a bead on a moving substrate

Another problem that includes a three-dimensional dynamic contact lines is the extrusion of a liquid onto a moving substrate. We refer to this as the 'bead laydown' problem. Examples of this type of process can be found in fields as diverse as free-casting of complex parts to food processing. It is a challenging problem because the contact angle on the horseshoe-shaped contact line changes continually from a maximum value at the leading edge, where the motion of the substrate is perpendicular to the line, to a static value downstream of the nozzle, where the motion of the substrate is parallel to the contact line and the fluid moves as a rigid body along with the substrate.

Figure 6 depicts the geometry and the starting shape of the finite element mesh. The proportions shown are based upon an actual experimental apparatus with a $D = 0.127$ cm nozzle diameter. The nozzle lies $0.89D$ above the substrate and the horizontal portion of the mesh extends approximately $5D$ downstream of the nozzle. The $y = 0$ plane is a symmetry plane, and this was exploited to reduce the number of unknowns by solving only one-half of the problem. The mesh shown in Figure 6 contains 2691 elements, 3296 nodal points, and 23 072 unknown degrees of freedom.

The boundary conditions applied to this mesh are depicted in Plate 1. No-slip is applied on the walls of the nozzle. The kinematic condition (17) is enforced on the free surface as shown; the free surface deforms to satisfy this constraint. On the symmetry plane, zero normal velocity is enforced; otherwise, the fluid is allowed to slip tangentially on this boundary. On the underside of the mesh, where the fluid adheres to the moving substrate, no-slip between substrate and fluid is enforced except along a narrow band of elements adjacent to the contact line. As in the case of the droplet problem, a Navier slip condition is applied in this region. The conditions applied along the contact line to the momentum and pseudo-solid mesh equations are the same as those applied in the droplet problem but changed for steady state conditions.

A study examining the effect of several input parameters was conducted. The fluid modeled was based upon a silicon oil standard fluid with density of 1 $\mathrm{g\,cm^{-3}}$ and viscosity 1024 P. These properties were fixed, but the surface tension was varied to obtain different values of the global capillary number. The surface tension values considered were in general much larger than the actual fluid's for reasons that will be discussed below. Contact angle data were not available. Instead, the parameters of the contact angle model were varied in order to study the effects of the contact angle model. However, the parameters were not varied independently. For a given static contact angle, the slope parameter c_T was adjusted so the contact angle at the leading edge of the bead would always be 175°. This was done to reflect the experimental observation for this highly viscous fluid, which the contact angle at the leading edge was generally very close to 180°.

The results of this parameter study are shown in Figures 7–9. Each figure gives three different views of the free surface shape: from the left to right, front, side, and underside or webside. The underside views are presented in a split view format; one half the domain is shown in 'hidden view' format, but the other half is shown in 'wire-frame' format. This allows for locating the contact line with respect to the inlet nozzle.

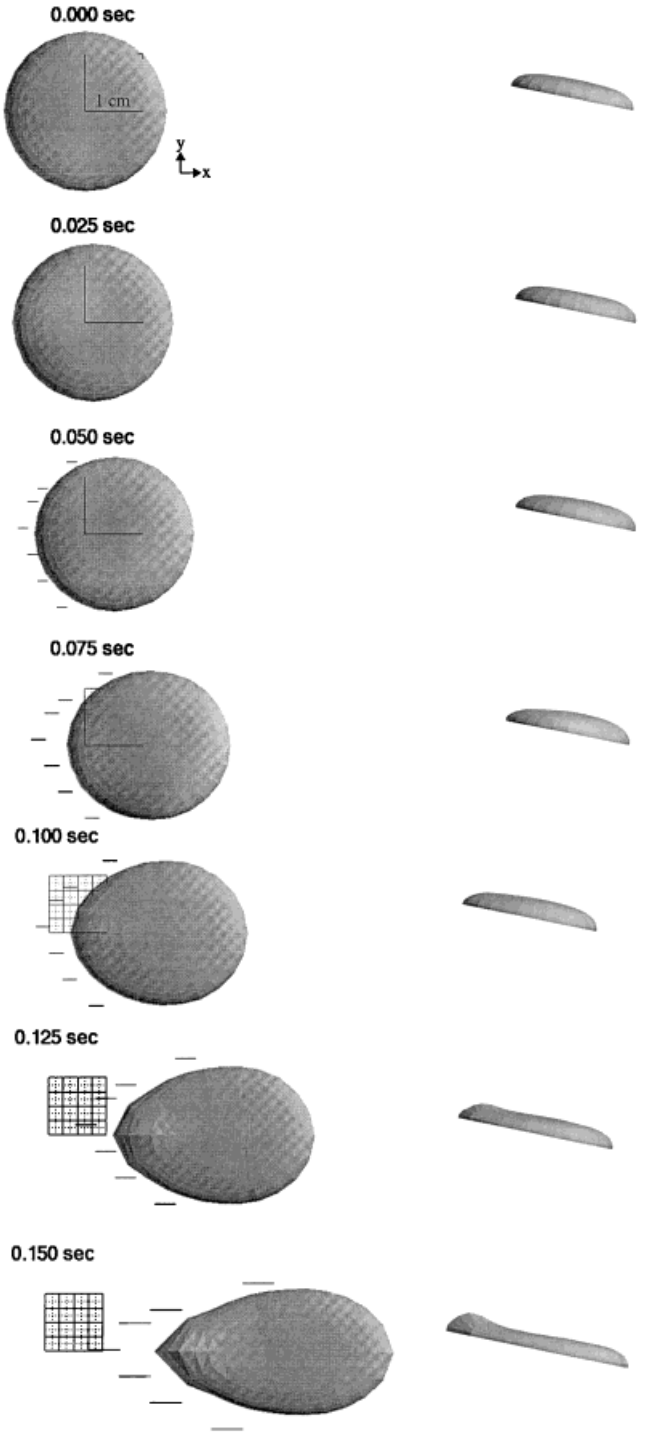

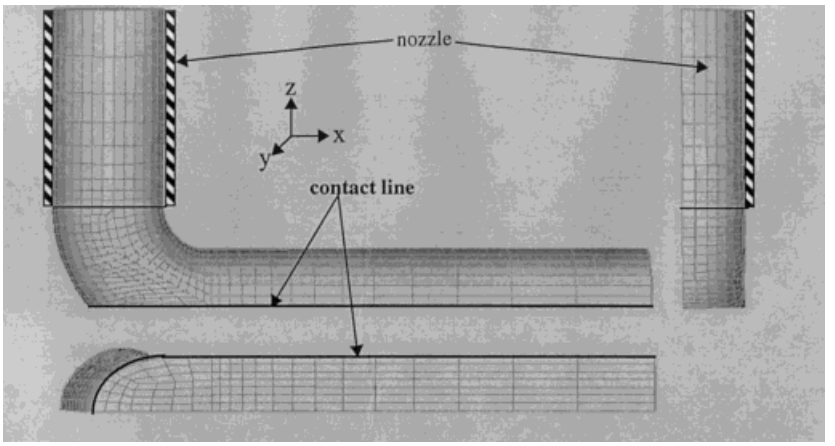

Figure 6. Mesh and initial undeformed geometry used in bead laydown computation. Since $y = 0$ is a symmetry plane, only one half the problem needed to be solved.

Figure 7 shows the effect of changing the ratio of the average inlet liquid velocity to substrate speed on the steady free surface shape. The static contact angle was fixed at 110°. The capillary number based upon the speed of the web was 1.0. The ratio of average inlet liquid velocity to web speed presented are, from top to bottom, 1.0, 1.6, 2.5, and 3.2 respectively. The behavior is generally what one expects. As the inlet flow is increased with a fixed web speed, the fluid tends to pile up around the nozzle, billowing to the sides and ahead of the nozzle. At the highest ratio, the contact line has advanced almost one-half a diameter ahead of the nozzle. In addition, the contact line contracts back towards the symmetry plane at a distance downstream from the nozzle. This is accompanied by the ridgeline of the bead rising to a height that is greater than the gap between nozzle and substrate. This behavior is a consequence of the relatively high surface tension present, which tends to contract the bead from its spayed out configuration in the vicinity of the nozzle to a more hemispherical configuration downstream where the influence of the nozzle has disappointed.

Figure 8 shows the influence of surface tension on the free surface shape. At a speed ratio of 1.6, the figure depicts the response at capillary number of 0.5, 1.0, and 2.0. Again the static contact angle was fixed at 110°. Although the changes in the free surface shape are smaller than the previous case, it is clear and expected that the liquid tends to spread out more as the capillary number increases, i.e., as an effect of the diminished surface tension. It is worth noting that convergent results were not obtained for Ca greater than approximately 2.0. Surface tension has the effect of stabilizing the free surface; as it is decreased, oscillations tend to appear in the free surface. This was especially true for the mesh used in this study. Because

Figure 5. Planform and side views of initial droplet acceleration down 30° inclined plane at several time points. For scale, the grid appearing on the views is 1 cm on a side. Note the distortion of the mesh at the trailing edge at the last time values.

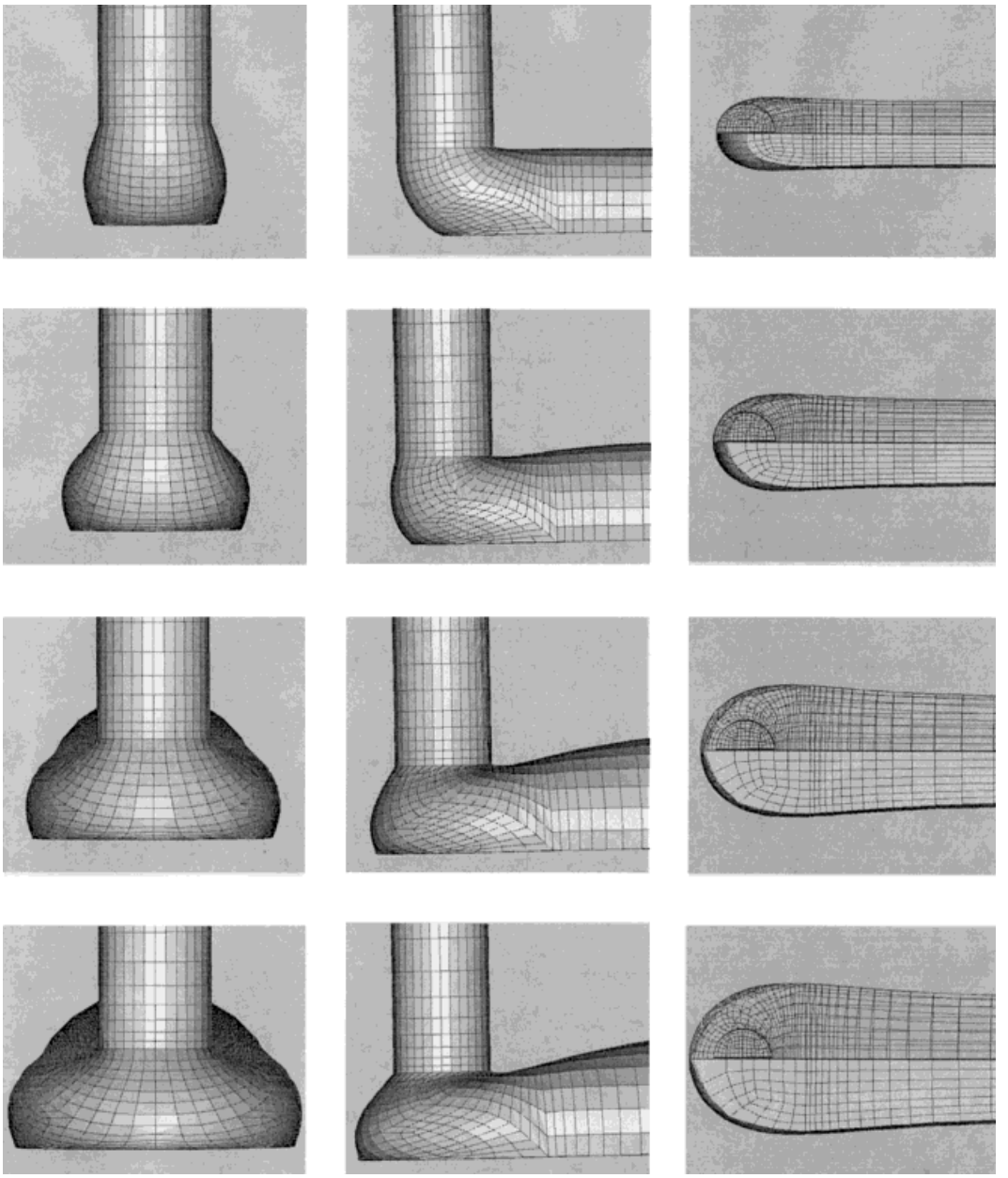

Figure 7. Effect of average inlet fluid velocity to web speed ratio on free surface shape at $Ca = 1.0$. From top to bottom, ratio values are 1.0, 1.6, 2.5, and 3.2.

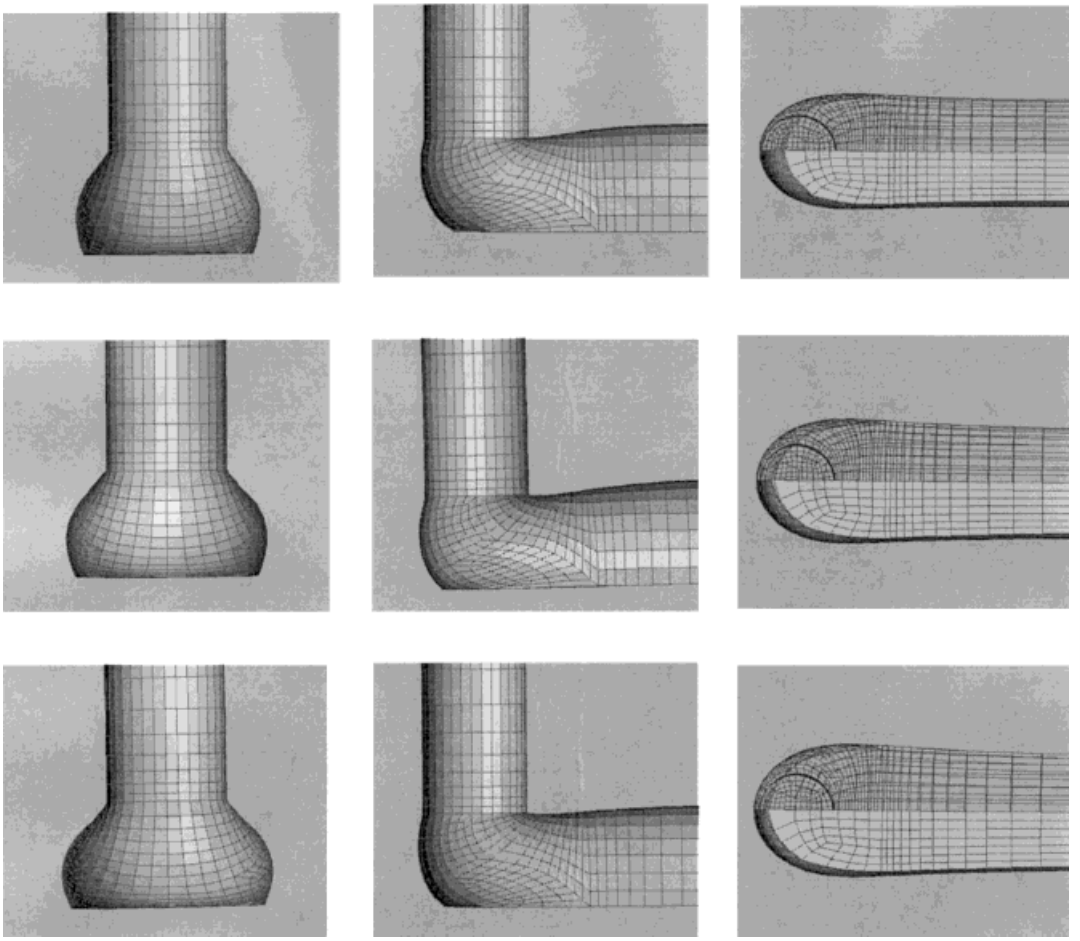

Figure 8. Effect of surface tension on shape of bead laydown free surface shape. From top to bottom, global capillary numbers are 0.5, 1.0, and 2.0. The inlet to web velocity ratio is 1.6.

of the large distortion on the free surface, the elements at the leading edge near the contact line had become large in the dimensions parallel to the web but very narrow in the direction perpendicular to it. Oscillations were observed on a portion of the free surface including these elements. This is the reason that the actual surface tension of the silicon oil could not be used; its high viscosity resulted in too large a capillary number. Although not undertaken here, this problem may be alleviated by better refinement of the area nearest the contact line.

Finally, Figure 9 shows the influence of the static contact angle. Here, the slope of the contact angle model was not set to ensure a specific contact angle at the leading edge, but instead held constant. The ratio of inlet average liquid velocity to web was again 1.6 and the surface tension of the fluid was set to give a capillary number of 1.0. The views shown in this

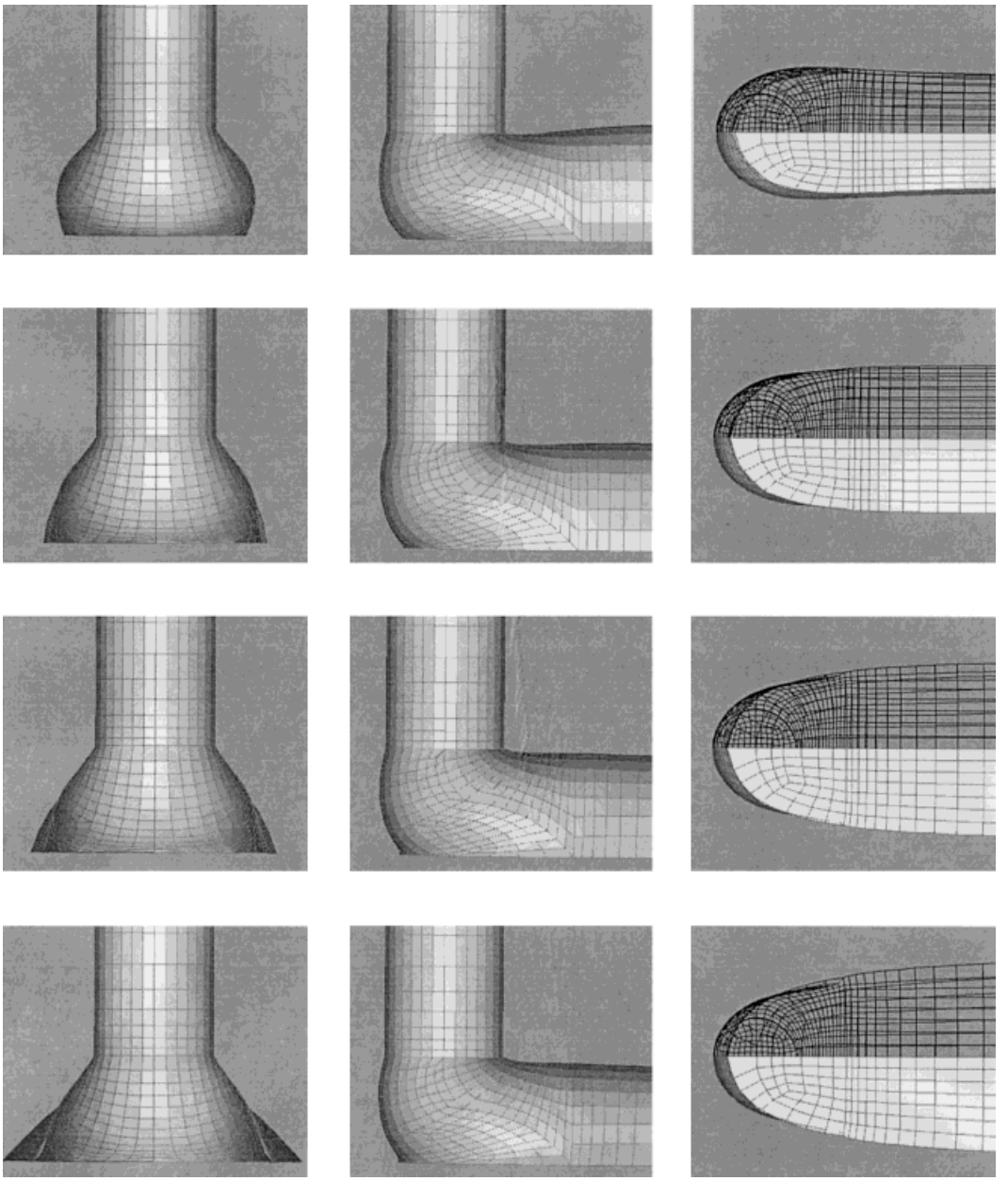

Figure 9. Effect of static contact angle on shape of bead laydown free surface shape. From top to bottom, static contact angle values are 110°, 80°, 60°, and 45°. The inlet velocity to web velocity ratio is 1.6.

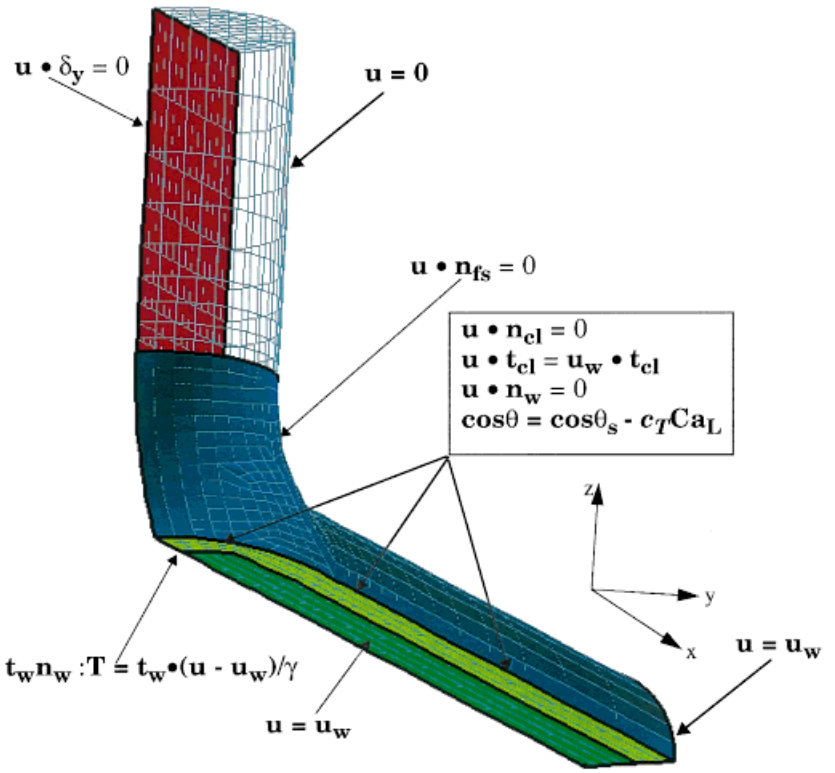

Plate 1. Boundary conditions applied to bead laydown domain.

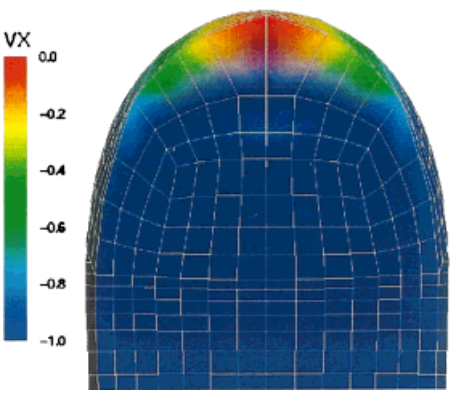

Plate 2. Axial velocity component parallel to motion of web on interface plane between fluid and substrate. View is at the underside. Ratio of inlet average velocity to web speed: 3.2, global capillary number: 1.3.

figure are for static contact angles of 110°, 80°, 60°, and 45°, top to bottom. The front view clearly shows the strong influence of this parameter at the downstream outlet, where the normal contact line velocity is smallest. Near the nozzle its influence is less, although still noticeable. The results are also in agreement with our expectations: the liquid spreads out to a greater extent for the lower static angles, which imply a greater propensity for wetting. The influence of the slope parameter c_T was also conducted; however, it was found that it did not have a tremendous effect on the overall shape of the free surface.

4.4. Comparison with experiments

We have made some preliminary steps towards direct comparison of these simulations with experiment. A second standard silicon oil was chosen for visualization. Its viscosity is 126.4 P. Its density was found to be 1 $\mathrm{g\,cm^{-3}}$ and a value of 20 $\mathrm{dyn\,cm^{-1}}$ for surface tension was obtained from the literature as a typical value [23]. Because of its (relatively) low viscosity, consistency could be achieved between experimental global capillary numbers and those accessible to numerical computations (unlike the previous set of computations). By extruding this fluid onto a moving glass platform, records could be made of the shape of the free surface and the shape and location of the dynamic contact line over a range of flow rates and table speeds. Figure 10 shows the results at one flow rate and table speed. The average inlet velocity was 0.64 $\mathrm{cm\,s^{-1}}$ and the web speed was 0.2 $\mathrm{cm\,s^{-1}}$, i.e., the ratio of inlet liquid flow rate to web speed was 3.2. The inside nozzle diameter in this case was 0.137 cm. The capillary number computed from the speed of the web was 1.3. A 90° static contact angle was used in the simulation. This value was chosen because, lacking any additional data, it would have the smallest potential error, namely 90°, of any other value. The value for c_T was obtained from the static contact angle as explained above.

In general, the qualitative shape of the computed contact line is similar to the experimental observation in that both are smoothly varying and parabola-shaped. However, the calculated contact line lies well in advance of the nozzle exit. In contrast, the experimental contact line is almost directly below the upstream side of the nozzle exit. Further, the lateral spread of the computed contact line extends more than a nozzle diameter away from the centerline plane. The experimental contact line extends outward to a lesser extent. Comparison of bead ridge behind the nozzle cannot be made because the actual fluid has wetted up the backside of the nozzle obscuring this portion of the photo.

That the agreement is less than desirable is attributable to at least two possibilities. First, the distortion of the elements in the vicinity of the contact line leading edge (i.e., the front) has expanded the region where the Navier slip condition is applied to an extent that is probably unreasonable. Plate 2 shows the computed axial velocity of the fluid on the interface between fluid and moving web. Over most of the region this component is uniformly the web speed, as it should be, but over a significant region near the leading edge of the bead, it differs significantly from the web speed. This could have the effect of allowing the contact line to advance ahead of the nozzle contrary to the experimental evidence. Second, as noted above, the contact angle model is probably too simplistic. While it captures the gross features needed in a contact angle model, it probably fails to predict detailed dependencies on the wetting parameters. A more realistic behavior is depicted in Figure 11, where the contact angle changes

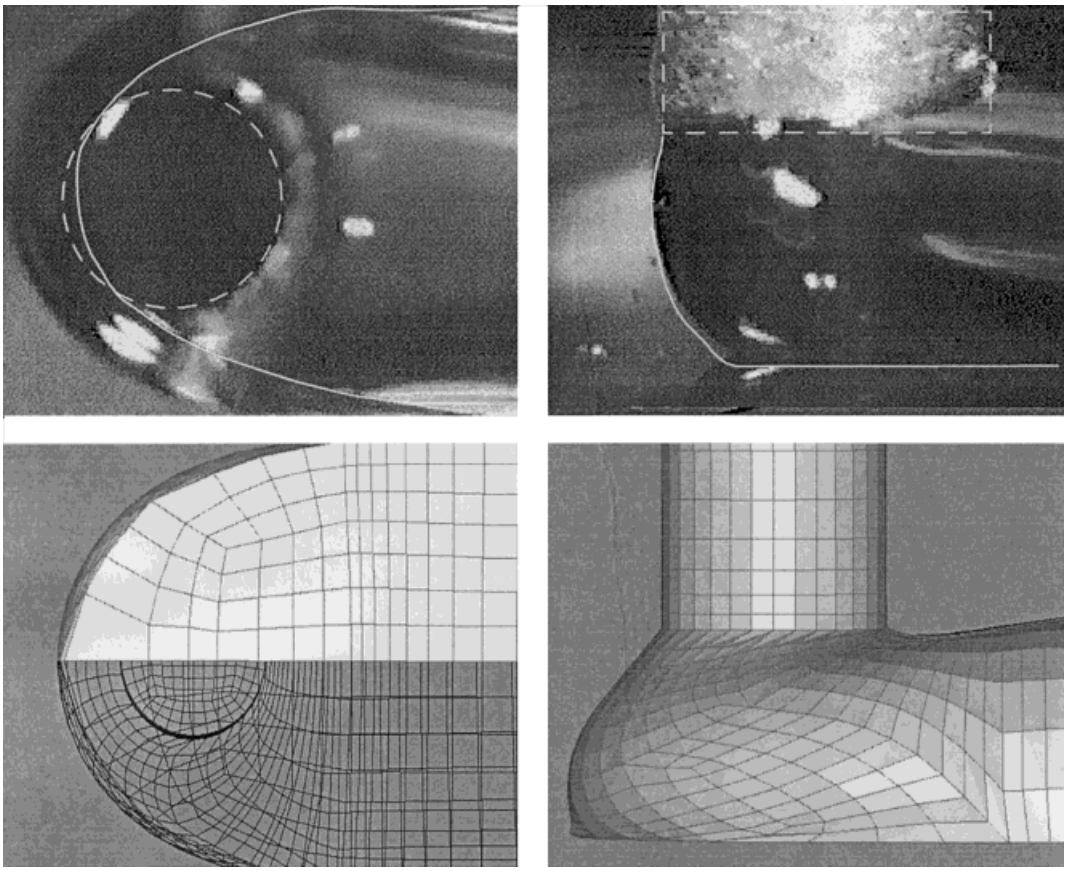

Figure 10. Comparison of experimental visualization of bead laydown free surface shape (top line) and corresponding computed results (bottom line). Ratio of inlet average velocity to web speed: 3.2, global capillary number: 1.3. White line indicates location of free surface and/or dynamic contact line.

rapidly for values of capillary number nearest to zero, but approaches constant values as the local capillary number becomes larger. Finally, we note that the parameters in the contact angle model were not based in any quantitative way on actual observations, but chosen for the most part arbitrarily. Given these limitations it is not surprising that agreement is lacking.

5. DISCUSSION

This work extends the body-fitted three-dimensional free surface method described in Part I [1], to include problems that possess three-dimensional static and dynamic wetting lines. Static wetting lines are described by single static contact angle along each wetting line. Dynamic wetting lines are more complicated for several reasons. The kinematic paradox needs to be

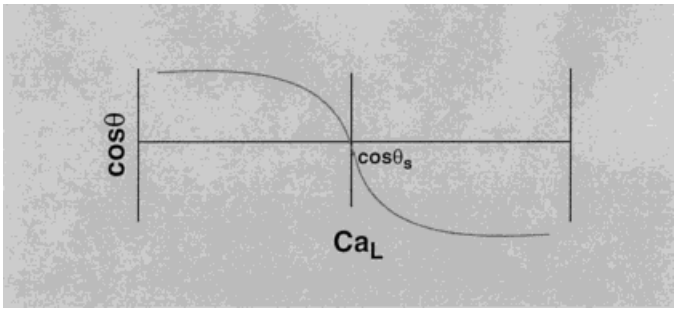

Figure 11. Sketch of features that would be appropriate to a more physically accurate contact angle model.

circumvented appropriately in three dimensions. Our approach is to assume that the fluid velocity at the wetting line, and the wetting line velocity itself, have the same normal component with respect to the substrate. The tangential component of the fluid velocity remains unaffected and is equivalent to the tangential component of the substrate velocity. Furthermore, for most practical problems in three dimensions, the dynamic contact angle must vary along at three-dimensional wetting line simply because the motion of the wetting line with respect to the substrate also changes. A model of the contact angle must allow a range of contact angles based upon the local rate of advancement or recession.

These modifications of the standard two-dimensional dynamic contact line formulation allow successful solution of the problems presented in this paper. The pseudo-solid approach to mesh motion, as explained in Part I [1], has shown considerable promise in three dimensions. Its ability to precisely locate the free surface and the wetting line has been instrumental in being able to apply these specialized and highly localized wetting line boundary conditions.

The sliding droplet computation represents an obvious application of our approach. It was observed that fluid would tend to shift to the downhill side of the droplet as time progressed. Further, the entire droplet became stretched in the flow direction but contracted in the direction transverse to the flow. Combined these effects resulted in the planform profile of the droplet evolving from an initial circular shape into the classic 'tear drop' shape. Another contact angle model, in particular one that included critical contact angle behavior, would result in a different shape [13]. We note also that at later times a hump of fluid appeared just in advance of the trailing edge. However, because the mesh there had become considerably distorted, we were unable to conclude that this was a true feature.

The bead laydown results have provided an opportunity to examine the shape of the wetting line to changes in operating and/or physical parameters. In general, the contact line was parabolic in form in the vicinity of the nozzle but evolving into a straight line parallel to the web motion downstream. Changing the flow rate did not alter this basic pattern except that for larger inlet velocities the contact line would become broader and further from the nozzle. We did note an important effect of surface tension on the downstream contact line behavior. For relatively large values of surface tension, the contact line would contract back towards the

centerline plane accompanied by the rise of the free surface ridgeline behind the nozzle. This imparted a 'paddle' shape to the overall contact line. As the surface tension decreased, this effect diminished. The static contact angle, however, had the most dramatic effect on the contact line shape. The smaller this parameter the further the contact line would spread downstream of the nozzle. Its effect was less pronounced in the region near the nozzle where the effects of the nozzle itself still dominate.

A number of issues still remain. The primary focus of this paper was development of an appropriate method for treating three-dimensional free surface problems with static and dynamic wetting lines. Having accomplished that, the next step is to address its deficiencies. The lack of stability of the free surface at higher capillary numbers is probably a result of inappropriately shaped elements. However, this premise needs to be verified on a better mesh. The lack of agreement with respect to the experimental visualization results is unfortunate but not unexpected given the focus on development of a numerical method. Better meshes and more appropriate contact angle models should improve agreement.

Nonetheless, the impact of these results should not be minimized. Static contact lines in three dimensions have received only a small amount of attention and dynamic contact lines even less. This should be contrasted with the vast amount of literature pertaining to two-dimensional dynamic contact lines. This paper represents a first in computational fluid mechanics in that there are few if any other computational studies of three-dimensional dynamic wetting lines. We believe that we have laid the theoretical and computational groundwork for continued exploration and development of this new area of computational science.

REFERENCES

1. Cairncross RA, Schunk PR, Baer TA, Sackinger PA, Rao RR. A finite element method for free surface flows of incompressible fluid in three dimensions. Part I: boundary-fitted mesh motion. *International Journal for Numerical Methods in Fluids* 2000; **33**: 375–403.
2. Adamson HW. *Physical Chemistry of Surfaces* (4th edition). Wiley: New York, 1982.
3. Dussan VEB. On the spreading of liquids on solid surfaces: static and dynamic contact lines. *Annual Review of Fluid Mechanics* 1979; **11**: 371.
4. Kistler SF. The fluid mechanics of curtain coating and other related viscous free surface flows with contact lines. PhD Thesis, University of Minnesota, 1984.
5. Christodoulou KN, Scriven LE. The fluid mechanics of slide coating. *Journal of Fluid Mechanics* 1989; **208**: 321.
6. Christodoulou KN, Kistler SF, Schunk PR. Advances in computational methods for free surface flows. In *Liquid Film Coating*, Kistler SF, Schweizer PM (eds). Chapman and Hall: London, 1997; 297–366.
7. Schunk PR, Scriven LE. Surfactant effects in coating processes. In *Liquid Film Coating*, Kistler SF, Schweizer PM (eds). Chapman and Hall: London, 1997; 495–536.
8. Lowndes J. The numerical simulation of the steady movement of a fluid meniscus in a capillary tube. *Journal of Fluid Mechanics* 1980; **101**: 631.
9. Zhou M-Y, Sheng P. Dynamics of immiscible-fluid displacement in a capillary tube. *Physics Reviews and Letters* 1990; **64**: 882.
10. Kistler SF, Zvan G. Hydrodynamic models of forced wetting in coating flows. 44th IS&T Conference, St. Paul, MN, 12–17 May, 1991.
11. Christodoulou KN, Scriven LE. The physics of slide coating, dynamic wetting, air entrainment. AICHE Spring National Meeting, Orlando, FL, 18–22 March, 1984.
12. Extrand CW, Kumagai Y. Liquid drops on an inclined plane: the relation between contact angles, drop shape, and retentive force. *Journal of Colloid and Interface Science* 1995; **170**: 515.
13. Dussan EB, Tao-Ping Chow R. On the ability of drops or bubbles to stick to non-horizontal surfaces of solids. *Journal of Fluid Mechanics* 1983; **137**: 1.

14. Dussan EB. On the ability of drops or bubbles to stick to non-horizontal surfaces of solids. Part 2. Small drops or bubbles having contact angles of arbitrary size. *Journal of Fluid Mechanics* 1985; **151**: 1.
15. Swartz LW, Eley RR. Simulation of droplet motion on low-energy and heterogeneous surfaces. *Journal of Colloid and Interface Science* 1998; **202**(1): 173.
16. Blake TD, Ruschak KJ. Wetting static and dynamic contact lines. In *Liquid Film Coating*, Kistler SF, Schweizer PM (eds). Chapman and Hall: London, 1997; 63–98.
17. Jiang SF, Oh SG, Slattery JC. Correlation for dynamic contact angle. *Journal of Colloid and Interface Science* 1979; **69**: 74.
18. Bracke M, De Voeght F, Joos P. The kinetics of wetting: the dynamic contact angle. *Progress in Colloidal and Polymer Science* 1989; **79**: 142.
19. Chen KC. Studies of multilayer slide coating and related processes. Ph.D. Dissertation, University of Minnesota, 1992.
20. Ngan CG, Dussan EB. On the nature of dynamic contact angle: an experimental study. *Journal of Fluid Mechanics* 1982; **118**: 27.
21. Kistler SF. Hydrodynamics of wetting. In *Wettability*, Berg JC (ed.). M. Dekker: New York, 1993; 311–429.
22. Brown RA. Finite-element methods for the calculation of capillary surfaces. *Journal of Computational Physics* 1979; **33**: 217.
23. Baeger R (ed). *CRC Handbook of Lubrication*. CRC Press: Boca Raton, FL, 1994.

